

UNIONS–3500 2D Cosmic Shear: IV. Cosmological Constraints in Configuration Space

L. W. K. Goh,^{1,2*} S. Guerrini³, C. Daley⁴, F. Hervas-Peters⁴, A. Wittje⁵, M. Kilbinger⁴, H. Hildebrandt⁵, M. J. Hudson^{6,7,8}, L. van Waerbeke⁹, T. de Boer¹⁰, E. Magnier¹⁰, TBD

¹ Institute for Astronomy, University of Edinburgh, Royal Observatory, Blackford Hill, Edinburgh EH9 3HJ, UK

² Higgs Centre for Theoretical Physics, School of Physics and Astronomy, The University of Edinburgh, Edinburgh EH9 3FD, UK

³ Université Paris Cité, Université Paris-Saclay, CEA, CNRS, AIM, 91191, Gif-sur-Yvette, France

⁴ Université Paris-Saclay, Université Paris Cité, CEA, CNRS, AIM, 91191, Gif-sur-Yvette, France

⁵ Ruhr University Bochum, Faculty of Physics and Astronomy, Astronomical Institute (AIRUB), German Centre for Cosmological Lensing, 44780 Bochum, Germany

⁶ Department of Physics and Astronomy, University of Waterloo, 200 University Avenue West, Waterloo, Ontario N2L 3G1, Canada

⁷ Waterloo Centre for Astrophysics, University of Waterloo, Waterloo, Ontario N2L 3G1, Canada

⁸ Perimeter Institute for Theoretical Physics, 31 Caroline St. North, Waterloo, ON N2L 2Y5, Canada

⁹ Department of Physics and Astronomy, University of British Columbia, 6224 Agricultural Road, V6T 1Z1, Vancouver, Canada

¹⁰ Institute for Astronomy, University of Hawaii, 2680 Woodlawn Drive, Honolulu HI 96822

Accepted XXX. Received YYY; in original form ZZZ

ABSTRACT

We present results from the configuration space cosmic shear analysis of the UNIONS galaxy catalogue.

Dear reader, please note that the current manuscript has been written up based on blind A of the redshift distribution. All sections up to Section 5 are ready for review (with the exception of Sect. 3.4).

Key words: Cosmology: observations—gravitational lensing: weak—cosmological parameters

1 INTRODUCTION

Since its first detection two and a half decades ago (Bacon et al. 2000; Kaiser et al. 2000; Van Waerbeke et al. 2000; Wittman et al. 2000), weak gravitational lensing has emerged as a powerful tool to probe the Universe, particularly the properties of its most elusive components: dark energy and dark matter. Weak lensing exploits the fact that along the line of sight, the observed shapes of background galaxies are distorted—or ‘sheared’—as their light is deflected by the intervening gravitational potential of foreground matter distributions. By measuring the shapes of these sheared galaxies, or more specifically the correlations between them, **these correlations trace the underlying dark matter distribution**, more commonly known as the large-scale structure (LSS) of the Universe.

An additional advantage of weak lensing as a cosmological probe is that it offers insight into the evolution of the LSS at low redshifts and on relatively small scales, thus **making it highly complementary to** other cosmological probes like the cosmic microwave background (CMB) and baryonic acoustic oscillations (BAOs). **Weak lensing best constrains the combination of σ_8** , the amplitude of clustering at a scale of $8 h^{-1}$ Mpc, and the present-day total matter density Ω_m , often captured in a single parameter $S_8 \equiv \sigma_8 \sqrt{\Omega_m / 0.3}$.

There have been several galaxy surveys dedicated to weak lensing science, with Stage III surveys (see Albrecht et al. 2006, for a definition of the different galaxy survey ‘stages’) such as the Kilo-Degree Survey (KiDS; Wright et al. 2024) and the Dark Energy Survey (DES;

Bechtol et al. 2025) publishing their last data releases, as well as the Hyper-Suprime Cam survey releasing their latest data set comprising three years’ worth of observations (HSC Y3; Li et al. 2022). In recent years, low-redshift weak lensing and galaxy clustering analyses have consistently favoured a lower value of S_8 than that inferred from high-redshift CMB measurements (e.g. Planck Collaboration 2020b), with discrepancies at the level of 1–3 σ (see Di Valentino et al. 2025, for example for an in-depth review). Whether this tension signals new physics or simply reflects residual systematics, the current cosmological landscape appears poised for an answer. Most recently, the KiDS-Legacy cosmic shear analysis (Wright et al. 2025a), which incorporates improved modelling of systematic effects, together with a re-analysis of HSC Y3 data using clustering-redshift techniques (Chopin de Janvry et al. 2025), seems to suggest a possible resolution.

Stage IV surveys including *Euclid* (Euclid Collaboration: Mellier et al. 2025) and the Vera C. Rubin Observatory’s Legacy Survey of Space and Time (LSST; Ivezić et al. 2019) have begun operations and are expected to publish their first data releases in the coming years. With this new generation of experiments, sub-percent precision on key cosmological measurements becomes achievable, making the coming decade an exciting one for both the quantity and quality of observational data.

Into this landscape comes the Ultraviolet Near Infrared Optical Northern Survey (UNIONS; Gwyn et al. 2025), an ongoing Stage III survey targeting over 5,000 deg² of the northern sky. This paper, along with four accompanying papers, constitutes the first major UNIONS cosmic shear analysis, based on 3,500 deg² of data accumulated

* E-mail: lgoh@roe.ac.uk

over more than five years of coordinated observations from three wide-field telescopes in Hawai'i.

UNIONS *r*-band imaging with the Canada-France Hawai'i Telescope (CFHT) enables high-quality weak lensing measurements through its excellent seeing. We present configuration-space cosmological constraints from the largest northern-hemisphere weak lensing data set to date, complementing the preceding Stage III analyses (Abbott et al. 2022; Dalal et al. 2023; Li et al. 2023a; Abbott et al. 2023; Anbjagane et al. 2025; Wright et al. 2025a).

This paper is structured as follows: Sect. 2 provides a brief overview of the UNIONS galaxy catalogue. In Sect. 3, we outline the theoretical modelling of the cosmic shear two-point correlation function (2PCF), the central probe used in this work, along with the additional components required for a complete cosmic shear analysis, including systematic error modelling, the covariance matrix and redshift distribution estimation, and a brief outline of external data sets integrated into the analysis. In Sect. 4, we describe our inference pipeline and detail how we take into account systematic effects and define our scale cuts. In Sect. 5 we present our results in terms of the marginalised cosmological parameter constraints, across various analysis setups and data set combinations. Finally, in Sect. 6 we offer our conclusions.

Table 1 provides a summary of the accompanying papers in this release: catalogue construction (Paper I; Hervas Peters et al. 2026a); image simulations and shear calibration (Paper II; Hervas Peters et al. 2026b); *B*-mode validation (Paper III; Daley et al. 2026); cosmological constraints in configuration space (Paper IV; this work); and lastly cosmological constraints in harmonic space (Paper V; Guerrini et al. 2026).

2 THE UNIONS DATA SET

UNIONS combines multi-band photometric images from multiple telescopes. The Canada-France Imaging Survey (CFIS) provides *u*– and *r*–band images from CFHT. The shape measurement of galaxies relies on high-quality images taken in the *r* band, which benefit from exquisite seeing of ~ 0.7 arcsec, making it ideal for weak lensing science. The Panoramic Survey Telescope and Rapid Response System (Pan-STARRS) provides imaging in the *i* and *z* bands. The Subaru telescope also takes images in the *z* band within the framework of the WISHES (Wide Imaging with Subaru HSC of the Euclid Sky) programme, and in the *g* band through the WHIGS (Waterloo Hawai'i Ifa Survey) programme. UNIONS provides wide-field multiband photometry over the optical bands, contributing to *Euclid*'s photometric redshifts on the northern sky. An extension collects data in all five bands down to 15° in declination. For a full review of UNIONS and its survey strategies, see Gwyn et al. (2025).

2.1 UNIONS weak lensing catalogue

This paper presents the first cosmological parameter estimation using the UNIONS 2D weak lensing catalogue. Since this galaxy sample comprises images collected specifically in the *r* band, we do not yet possess colour information to construct multiple tomographic bins; this analysis therefore relies on a single, two-dimensional redshift distribution (see Sect. 3.3 for more details).

The shape measurement was performed with ShapePipe (Farrens et al. 2022; Guinot et al. 2022), which also incorporates the galaxy point-spread function (PSF) modelling based on PSFEx (Bertin 2011). Our lensing sample gathers data collected until the end of 2022, and is composed of over 61.4 million galaxies totalling an area

of $3,500 \text{ deg}^2$, corresponding to $2,894 \text{ deg}^2$ of effective area after masking. The shapes of the galaxies were measured using ngmix (Sheldon 2015) and the calibration of the galaxy ellipticities was performed using Metacalibration (Huff & Mandelbaum 2017; Sheldon & Huff 2017). This gives an effective galaxy number density of 4.96 arcmin^{-2} and per-component shape noise of $\sigma_e = 0.27$. Calibrated shapes using Metacalibration are saved but undergo a second correction step to remove residual per-component PSF leakage, an empirical process adapted from Li et al. (2023b). The catalogue contains two sets of the spin-2 ellipticities for each galaxy, e_1 and e_2 , corrected for the per-component additive biases c_1 and c_2 . Specific details on the PSF fitting and validation, shape measurement and leakage correction methods can be found in Paper I.

Additionally, different size cuts and masking schemes were explored before converging on the one employed to create the final UNIONS shear catalogue. In its current version, a size cut of $r_{\text{h,gal}}/r_{\text{h,psf}} > 0.7$ was applied, where r_{h} is defined as the half-light radius, effectively discarding objects with sizes comparable to the PSF. The effective mask is an amalgamation of the flags generated during MegaPipe processing, and post-processing pixel-based and area-based masking, as well as the ShapePipe selection criteria of $n_{\text{epoch}} \geq 2$ and $n_{\text{point}} \geq 3$ (representing the number of epochs observed for each object, and the number of pointings for each object, respectively). In total, this nominally excludes objects detected as blends, regions around Messier and NGC objects, bright stars, stellar halos, diffraction spikes, defects, and cosmic rays. We also explored a more comprehensive masking of halo-like emissions around faint and bright stars (beyond the stellar halos already flagged by MegaPipe), but B-mode null tests showed this additional masking introduced systematic contamination; this additional masking was not applied. For an in-depth study of the impact of size cuts and masking schemes, we refer the reader to Paper I and Paper III.

3 MODELLING

We detail how we model the cosmic shear 2-point correlation function (2PCF), including validation tests for systematic effects, the covariance model, and the redshift distribution.

3.1 Cosmic shear 2-point correlation function

In the regime of weak lensing, the magnitude of the distortion of individual galaxy images is too small to be detected. Hence, a large ensemble of galaxies must be analysed together by calculating the correlation of the measured shapes between pairs of galaxies. There exist several summary statistics that capture this information, most notably the two-point correlation functions in configuration space $\xi_{\pm}^{ij}(\theta)$, and the angular power spectra C_{ℓ}^{ij} in Fourier or harmonic space. In principle, these two statistics capture similar information on the sky, albeit with different sensitivities to scales and masking effects. For comprehensive reviews on weak lensing theory and methodologies, see for example Bartelmann & Schneider (2001) and Kilbinger (2015). For results on the cosmic shear analysis of UNIONS in Fourier space, we refer the reader to Paper V.

The cosmic shear 2PCF is expressed as the expectation value of the tangential and cross components of the galaxy shear signal, γ_t and γ_x respectively, squared (Kaiser 1992),

$$\xi_{\pm}(\theta) = \langle \gamma_t \gamma_t \rangle(\theta) \pm \langle \gamma_x \gamma_x \rangle(\theta), \quad (1)$$

which is a function of θ , the angle of separation between a pair of galaxies on the sky. The $\xi_{\pm}(\theta)$ functions can also be derived from

Table 1. List of associated publications in this coordinated UNIONS release.

Paper Index	Author	Title
I	Hervas Peters et al. (2026a)	Weak lensing catalogues
II	Hervas Peters et al. (2026b)	Image simulations and shear calibrations
III	Daley et al. (2026)	B-mode validation and comparison
IV	This work	Cosmological constraints in configuration space
V	Guerrini et al. (2026)	Cosmological constraints in harmonic space

their Fourier space counterpart by a Hankel transform, such that the 2PCF between tomographic bins i and j , assuming the Limber and flat-sky approximations, is given by (Kaiser 1998)

$$\xi_{\pm}^{ij}(\theta) = \int_0^{\infty} \frac{\ell d\ell}{2\pi} J_{0,4}(\theta\ell) C_{\ell}^{ij}, \quad (2)$$

where J_n is the n th-order spherical Bessel function of the first kind, with $n = 0$ for ξ_+ and $n = 4$ for ξ_- . For completeness, the cosmic shear power spectrum C_{ℓ}^{ij} is given by the integral of the product of the lensing efficiency as a function of the comoving distance $q_i(\chi)$, and the nonlinear matter power spectrum $P_{\text{NL}}(k, z(\chi))$,

$$C_{\ell}^{ij} = \int_0^{\chi_H} d\chi \frac{q^i(\chi) q^j(\chi)}{\chi^2} P_{\text{NL}}(k, z(\chi)), \quad (3)$$

where χ_H is the comoving distance to the horizon, and

$$q^i(\chi) = \frac{3}{2} \Omega_m \frac{H_0}{c^2} \int_{\chi}^{\chi_H} d\chi' n^i(\chi') \frac{\chi - \chi'}{\chi'}. \quad (4)$$

Here $H_0 = 100h \text{ km s}^{-1}\text{Mpc}^{-1}$ is the Hubble constant and $n^i(\chi')$ is the galaxy redshift distribution. Since we are only working with one tomographic bin in this analysis (see Sect. 3.3 for more details), we hereafter drop the ij notation, automatically assuming that the 2PCF in question refers to the auto-correlation of the single bin (i.e. $i = j = 1$).

The cosmic shear observable is the observed ellipticity of a galaxy \mathbf{e}^{obs} , which is the sum of its intrinsic ellipticity \mathbf{e}^s and shear $\boldsymbol{\gamma}$ (boldface denotes spin-2 quantities):

$$\mathbf{e}^{\text{obs}} = \mathbf{e}^s + \boldsymbol{\gamma}. \quad (5)$$

Following the notation of Schneider et al. (2002), we define the angular bin width as $\Delta\theta$ and $\Delta_{\theta}(\phi) = 1$ for $\theta - \Delta\theta/2 \leq \phi \leq \theta + \Delta\theta/2$ and zero elsewhere. The 2PCF estimator for a galaxy pair i, j at separation $|\theta_i - \theta_j|$ is

$$\hat{\xi}_{\pm}(\theta) = \frac{\sum_{ij} w_i w_j (e_{it} e_{jt} \pm e_{ix} e_{jx}) \Delta_{\theta}(|\theta_i - \theta_j|)}{N_p^{ij}(\theta)}, \quad (6)$$

where w is the galaxy weight, computed during the shape measurement step, and $N_p^{ij}(\theta)$ is the effective number of galaxy pairs in the galaxy bin.

In Fig. 1 we present the $\hat{\xi}_{\pm}(\theta)$ data vectors computed by TreeCorr (Jarvis et al. 2004), where we have binned the separation angle θ into 20 logarithmically-spaced bins over 1–250 arcmin. We also include their associated uncertainties given by the diagonals of the covariance matrix, which is detailed in Sect. 3.5.

3.2 Systematic effects and validation tests

We assess the robustness of our data vectors to systematic measurement effects, focusing on PSF modelling, configuration-space E/B -mode decomposition, and COSEBIS (Schneider et al. 2010; Asgari et al. 2012). These tests also drove the catalogue version evolution that led to the fiducial sample used here.

3.2.1 PSF systematic effects

The shear signal of a galaxy is estimated from its observed ellipticity. However, this measurement is often noisy, since it is contaminated by the PSF of the instrument. PSF leakage and mismodelling can contribute to the observed galaxy ellipticity in the form of an additive bias factor, $\mathbf{e}^{\text{PSF,sys}}$, such that

$$\mathbf{e}^{\text{obs}} = \mathbf{e}^s + \mathbf{e}^{\text{PSF,sys}} + \boldsymbol{\gamma}. \quad (7)$$

Quantifying this bias is essential for recovering an unbiased shear signal. A commonly used model for PSF leakage is Paulin-Henriksson et al. (2008); Jarvis et al. (2016)

$$\mathbf{e}^{\text{PSF,sys}} = \alpha_{\text{PSF}} \mathbf{e}^p + \beta_{\text{PSF}} \delta \mathbf{e}^p + \eta_{\text{PSF}} \delta \mathbf{T}^p, \quad (8)$$

where α_{PSF} , β_{PSF} and η_{PSF} are constant free parameters, \mathbf{e}^p is the ellipticity of the PSF model, $\delta \mathbf{e}^p = \mathbf{e}^* - \mathbf{e}^p$ is the PSF ellipticity residual and $\delta \mathbf{T}^p = \mathbf{e}^*(T^* - T^p)/T^*$ is the PSF size residual. We use the superscript ‘p’ to refer to the properties of the PSF (size or ellipticity), and ‘*’ to denote those of point-like sources (also referred to as stars) which, by convention, have zero PSF. Residual terms can only be evaluated at the positions of the stars.

The PSF-PSF and galaxy-PSF 2PCFs can be used to derive the amplitude of the leakage bias in the measured galaxy-galaxy correlation function. This is done by estimating the ρ statistics (introduced by Rowe 2010; Jarvis et al. 2016), representing PSF-PSF correlations, and τ statistics (introduced by Hamana et al. 2020; Giblin et al. 2021; Gatti et al. 2021), quantifying galaxy-PSF correlations, directly from the data. They are respectively given by (where we have dropped the ‘PSF’ subscript in α, β and η for clarity of notation)

$$\begin{aligned} \rho_0(\theta) &= \langle \mathbf{e}^p \mathbf{e}^p \rangle(\theta), & \rho_1(\theta) &= \langle \delta \mathbf{e}^p \delta \mathbf{e}^p \rangle(\theta), \\ \rho_2(\theta) &= \langle \mathbf{e}^p \delta \mathbf{e}^p \rangle(\theta), & \rho_3(\theta) &= \langle \delta \mathbf{T}^p \delta \mathbf{T}^p \rangle(\theta), \\ \rho_4(\theta) &= \langle \delta \mathbf{e}^p \delta \mathbf{T}^p \rangle(\theta), & \rho_5(\theta) &= \langle \mathbf{e}^p \delta \mathbf{T}^p \rangle(\theta), \end{aligned} \quad (9)$$

and

$$\begin{aligned} \tau_0(\theta) &= \langle \mathbf{e} \mathbf{e}^p \rangle(\theta) & = \alpha \rho_0(\theta) + \beta \rho_2(\theta) + \eta \rho_5(\theta), \\ \tau_2(\theta) &= \langle \mathbf{e} \delta \mathbf{e}^p \rangle(\theta) & = \alpha \rho_2(\theta) + \beta \rho_1(\theta) + \eta \rho_4(\theta), \\ \tau_5(\theta) &= \langle \mathbf{e} \delta \mathbf{T}^p \rangle(\theta) & = \alpha \rho_5(\theta) + \beta \rho_4(\theta) + \eta \rho_3(\theta). \end{aligned} \quad (10)$$

The second equality in Eq. (10) shows how α , β , and η are estimated from the $\rho(\theta)$ and $\tau(\theta)$ statistics. Further details can be found in Guerrini et al. (2025). We compute the 2PCF estimator of the PSF leakage as

$$\begin{aligned} \xi_{\pm}^{\text{PSF,sys}}(\theta) &= \alpha^2 \rho_0(\theta) + \beta^2 \rho_1(\theta) + \eta^2 \rho_3(\theta) \\ &\quad + 2\alpha\beta \rho_2(\theta) + 2\alpha\eta \rho_5(\theta) + 2\beta\eta \rho_4(\theta), \end{aligned} \quad (11)$$

such that the total estimated 2PCF signal is a sum of the true shear signal and a contribution from the PSF leakage,

$$\xi_{\pm}^{\text{obs}}(\theta; \alpha, \beta, \eta) = \xi_{\pm}^{\text{YY}}(\theta) + \xi_{\pm}^{\text{PSF,sys}}(\theta; \alpha, \beta, \eta). \quad (12)$$

Paper I measured the $\xi_{\pm}^{\text{PSF,sys}}(\theta)$ signal and found a non-negligible leakage bias on large scales for both the ξ_+ data vectors, despite

205

210

215

220

225

230

3

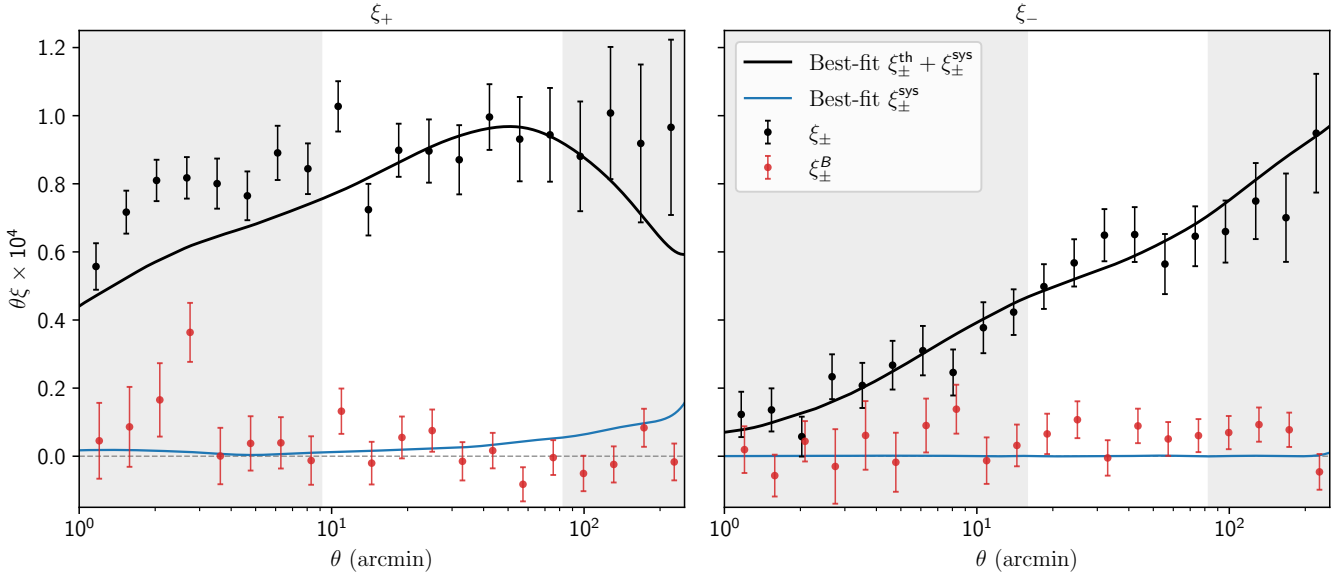


Figure 1. Real space 2PCF in black (left: ξ_+ , right: ξ_-) as a function of angular separation θ , with error bars computed from the diagonals of the covariance matrix. The grey sections denote the fiducial scale cuts employed for this analysis. The solid black line shows the best-fit model to the data, which includes both the cosmological and PSF-leakage signal. We also include B -mode estimates in red, as described in Sect. 3.2.2 and best-fit leakage systematics in blue, as described in Sect. 3.2.1. To be updated with latest fiducial scale cuts.

235 a noticeable improvement after applying an empirical leakage correction. The blue line when plotting the total data vectors in Fig. 1 corresponds to this PSF systematics contribution. We therefore model PSF systematics by additionally sampling the α and β parameters at the inference step (see Sect. 4.3 for details), fixing $\eta = 0$ since Guerrini et al. (2025) showed it is strongly correlated with α and that fixing η does not significantly modify the estimate of the leakage bias. We also use this systematic test to inform our scale cuts: requiring that the PSF leakage contribute less than 10% of the total signal gives an upper scale cut of 83 arcmin for both ξ_{\pm} .

240

245 3.2.2 E/B mode validation tests

Gravitational lensing produces a shear field that is curl-free to leading order; higher-order effects and intrinsic alignments can produce B -modes but remain below Stage III sensitivity (Schneider et al. 2022). Significant B modes are therefore evidence of residual systematics, and we use them as one of the determining factors for our scale cuts. For a detailed comparison of configuration- and harmonic-space B modes across catalogue variants (changes in PSF size cuts, masking), see Paper III; here we summarise the results for the fiducial catalogue used for the cosmic shear analysis.

We compute two B -mode statistics: pure-mode correlation functions $\xi_{\pm}^{E/B}(\theta)$ (Schneider et al. 2022) in configuration space; and the first six COSEBIs modes B_n . For each statistic, we calculate a probability to exceed (PTE) and require $\text{PTE} > 0.05$ to pass the null test. Preliminary blinded analyses with the initial selection (v1.4.5) passed configuration-space B -mode null tests but failed in harmonic space. We therefore introduced a more conservative size cut, removing approximately 25 per cent of galaxies and reducing n_{eff} from 6.48 to 4.96 arcmin $^{-2}$ and the per-component shape noise from 0.28 to 0.27. The stricter cut improved PSF leakage statistics, and the harmonic-space B -mode null tests passed.

Over the full angular range, COSEBIs (restricting to modes of $n \leq 6$) show significant B -modes with a PTE of 1.37×10^{-5} , while ξ_{\pm}^B

passes with a PTE of 0.42. After restricting to scales of 12–83 arcmin for both ξ_{\pm} signals, both null tests pass with PTEs of 0.78 and 0.20. These results informed the fiducial scale cuts (see Sect. 4.6).

270

3.3 Redshift distribution

We estimate the redshift distribution of our weak-lensing source sample based on the colour-redshift relation. Our shear catalogue used for this analysis, however, is not yet fully covered by the UNIONS multi-band photometry. To still use the colour-based approach for the redshift calibration, we use the spatial overlap between the UNIONS r -band data and the Canada–France–Hawaii Telescope Lensing Survey (CFHTLenS; Heymans et al. 2012; Erben et al. 2013) W3 field, which covers 44.2 deg 2 . CFHTLenS provides significantly deeper $ugriz$ photometry (Hildebrandt et al. 2012) than UNIONS, such that essentially all detected sources have CFHTLenS counterparts. We therefore cross-match these sources to CFHTLenS and adopt the associated $ugriz$ magnitudes. The matched sample is assumed to trace the same underlying colour–redshift distribution as the full UNIONS population.

To calibrate the redshift distribution, we assemble a spectroscopic sample that occupies the same photometric space as the matched UNIONS-CFHTLenS sources. This sample combines data from three deep spectroscopic surveys: the DEEP2 Galaxy Redshift Survey (Newman et al. 2013); the VIMOS VLT Deep Survey (VVDS; Le Fèvre et al. 2005); and the Vimos Public Redshift Survey (VIPERS; Scoville et al. 2018). All of these surveys were observed with CFHTLenS-like $ugriz$ filters, enabling direct comparisons in colour–magnitude space. After applying standard survey-specific quality cuts, we obtain a clean and representative set of galaxies for training the photometric–redshift calibration.

Using the multi-band photometry of the spectroscopic sample, we train a self-organising map (SOM; Kohonen 1982), which clusters galaxies based on their positions in the multi-dimensional magnitude space (Masters et al. 2015; Wright et al. 2020). The initial SOM

275

280

285

290

295

300

is defined on a 101×101 grid (also known as cells), providing a fine-grained tiling of colour–magnitude space. For robust statistical sampling, we subsequently hierarchically cluster the SOM into approximately 5000 effective resolution elements. This preserves the structure of the photometric manifold while ensuring that each region contains a sufficient number of spectroscopic objects for more robust mean statistics.

We then populate the SOM with the UNIONS weak-lensing sources by assigning each galaxy to its best-matching SOM cell based on its $ugriz$ photometry. Each UNIONS galaxy carries two lensing-related weights: (i) the standard shear (shape) weight w^{shape} ; and (ii) an additional response weight w^R derived from a smoothed shear response (Myles et al. 2021).

The shear-response weight w^R is constructed as follows. We bin the UNIONS sources in a two-dimensional space defined by the signal-to-noise ratio (SNR) and the galaxy size parameter $T_{\text{gal}}/T_{\text{PSF}}$. The resulting $(\text{SNR}, T_{\text{gal}}/T_{\text{PSF}})$ plane (shown in Figure 3 of Paper I) is similar to the binning scheme presented in Gatti et al. (2021) and is used to compute the mean shear response $\langle R \rangle$ in each bin. Each galaxy is then assigned the corresponding mean response value of its bin, which we use as an additional multiplicative weight,

$$w_j^R = \langle R \rangle_{\text{bin}(j)}. \quad (13)$$

With these two weights, the SOM weight for cell i is defined as

$$w_i^{\text{SOM}} = \frac{\sum_{j \in i} w_j^{\text{shape}} w_j^R}{N_i^{\text{spec}}}, \quad (14)$$

where the numerator sums the weighted counts of UNIONS galaxies assigned to cell i , and the denominator is the number N_i^{spec} of spectroscopic calibration galaxies in that cell (Wright et al. 2020). This definition ensures that the spectroscopic sample is reweighted to match the effective distribution of sources contributing to the shear signal.

Finally, the redshift distribution of the UNIONS weak-lensing sample is obtained by applying the SOM weights to the spectroscopic redshift distributions in each cell:

$$n(z) = \sum_i w_i^{\text{SOM}} n_i^{\text{spec}}(z), \quad (15)$$

where $n_i^{\text{spec}}(z)$ is the redshift distribution of spectroscopic galaxies located in SOM cell i . To obtain a statistically robust estimate of the final redshift distribution, we conduct a bootstrap resampling over the spatially binned spectroscopic calibration sample. We generate 1000 jackknife realisations of $n(z)$ and adopt the mean of these realisations as our final estimate. The final calibrated $n(z)$ distribution is shown in Fig. 2.

3.4 Shear multiplicative bias

- TBD, reference to Hervas-Peters et al. sims paper

3.5 Covariance modelling

We calculate the covariance matrix between angular bins by taking into account the Gaussian (G), connected non-Gaussian (nG), and super sample covariance (SSC) contributions. In a tomographic analysis, the total covariance matrix of two angular power spectra $C_{\ell_1}^{ij}$

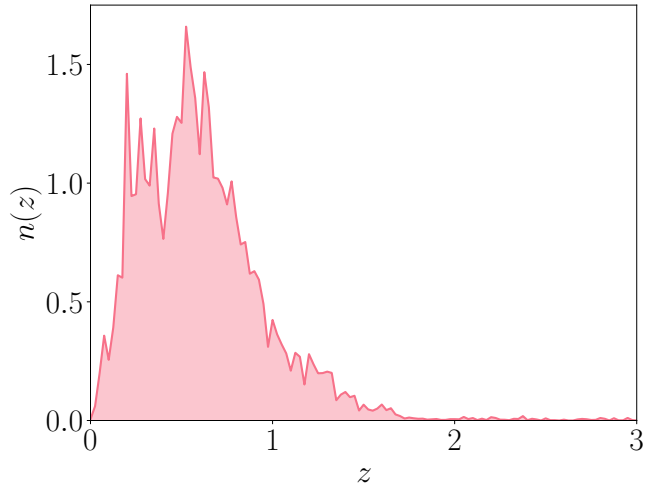


Figure 2. Normalised redshift distribution, $n(z)$.

and $C_{\ell_2}^{kl}$ in Fourier space is given by

$$\begin{aligned} \text{Cov} \left[C_{\ell_1}^{ij}, C_{\ell_2}^{kl} \right] = & \text{Cov}_G \left[C_{\ell_1}^{ij}, C_{\ell_2}^{kl} \right] + \text{Cov}_{\text{nG}} \left[C_{\ell_1}^{ij}, C_{\ell_2}^{kl} \right] + \\ & \text{Cov}_{\text{SSC}} \left[C_{\ell_1}^{ij}, C_{\ell_2}^{kl} \right]. \end{aligned} \quad (16)$$

Following the notation of Hu & Jain (2004), the Gaussian covariance term of any galaxy g or shear γ field can be expressed as

$$\begin{aligned} \text{Cov}_G = & [(2\ell_1 + 1) f_{\text{sky}} \Delta \ell]^{-1} \delta_{\ell_1 \ell_2}^K \times \\ & 4 \left\{ \left[C_{\ell_1}^{AC,ik} + N_{\ell_1}^{AC,ik} \right] \left[C_{\ell_2}^{BD,jl} + N_{\ell_2}^{BD,jl} \right] + \right. \\ & \left. \left[C_{\ell_1}^{AD,il} + N_{\ell_1}^{AD,il} \right] \left[C_{\ell_2}^{BC,jk} + N_{\ell_2}^{BC,jk} \right] \right\} \end{aligned} \quad (17)$$

where A, B, C, D represents either g or γ for the observed fraction of the sky f_{sky} , and noise power spectra N_{ij} . In the case of cosmic shear, $A = B = C = D = \gamma$, hence it is simply $N_{\ell}^{\gamma\gamma,ij} = \frac{\sigma_e^2}{2\bar{n}^i} \delta_{ij}^K$. Here \bar{n}^i is the mean galaxy number density of bin i and σ_e the shape noise, while δ_{ij}^K denotes the Kronecker delta. However, transitioning to small scales, the cosmic shear field becomes significantly non-Gaussian, leading to extra contributions arising from the connected four-point function of these fields. For the full expression of the connected non-Gaussian covariance terms, see for example Cooray & Sheth (2002) and Takada & Jain (2009).

Lastly, the SSC term, which captures the uncertainty due to a change in the background density at modes larger than the survey area, can be modelled following Takada & Hu (2013):

$$\begin{aligned} \text{Cov}_{\text{SSC}} \simeq & \frac{1}{f_{\text{sky}}} \int d\chi \frac{q^{A,i}(\chi) q^{B,j}(\chi) q^{C,k}(\chi) q^{D,l}(\chi)}{\chi^4} \times \\ & \frac{\partial P_{AB}(k_{\ell_1}, z)}{\partial \delta_b} \frac{\partial P_{CD}(k_{\ell_2}, z)}{\partial \delta_b} \sigma_b^2(z), \end{aligned} \quad (18)$$

where σ_b^2 is the covariance of the background density field δ_b within the survey window. In the case of a cosmic shear-only analysis, $q_i^{A,B,C,D}(\chi)$ is the cosmic shear lensing efficiency given in Eq. (4), and σ_b is given by (Lacasa & Rosenfeld 2016)

$$\sigma_b^2(z) = \frac{1}{2\pi^2} \int dk k^2 P_L(k, z) [j_0(kr)]^2, \quad (19)$$

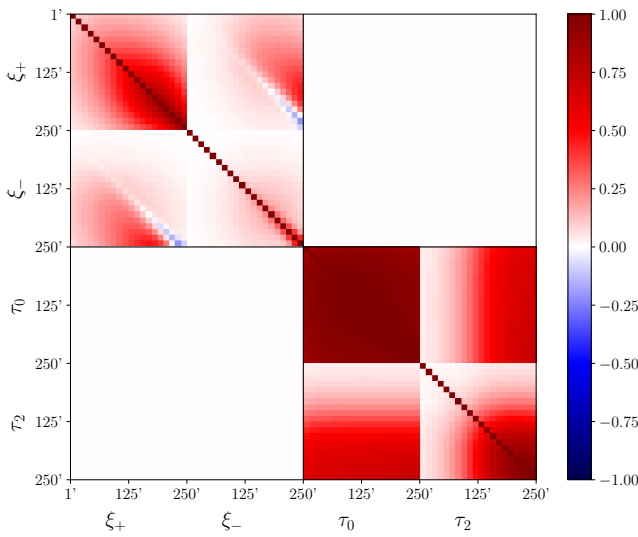


Figure 3. Correlation matrix of the two-point correlation functions, $\xi_{\pm}(\theta)$ and the $\tau_{0,2}(\theta)$ PSF leakage statistics (see Sect. 4.3).

where j_0 is the spherical Bessel function of zeroth order, and $P_L(k, z)$ refers to the linear matter power spectrum.

The covariance matrix for the 2PCF in configuration space follows from a Hankel transformation,

$$\text{Cov} \left(\xi_{\pm}^{ij}(\theta_1), \xi_{\pm}^{kl}(\theta_2) \right) = \frac{1}{4\pi^2} \times \int \frac{d\ell_1}{\ell_1} \int \frac{d\ell_2}{\ell_2} \ell_1^2 \ell_2^2 J_n(\ell_1 \theta_1) J_n(\ell_2 \theta_2) \times \left[\text{Cov} \left(C_{\ell_1}^{ij}, C_{\ell_2}^{kl} \right) \right], \quad (20)$$

370 where once again $n = 0$ for ξ_+ and $n = 4$ for ξ_- . We calculate our covariance matrix based on the above equations, using the CosmoCov software (Krause & Eifler 2017; Fang et al. 2020), where we have adopted the fiducial input cosmology following table 1 of Reischke et al. (2025). We plot the full correlation matrix (where $\text{Corr}_{ij} = \text{Cov}_{ij}/\sqrt{\text{Cov}_{ii} \times \text{Cov}_{jj}}$) in Fig. 3.

3.5.1 Effect of masking on covariance estimation

As was investigated in Troxel et al. (2018) and Friedrich et al. (2021), masking can result in a noncontiguous and patchy survey footprint, thus inducing additional uncertainties in the covariance matrix of the correlation functions. Following Schneider et al. (2002), the pure shape noise term of the covariance matrix in configuration space (referred to as $N_p^{\gamma\gamma}$ in the previous section) is given by

$$\text{Cov}^{\text{SN}} \left(\xi_{\pm}^{ij}(\theta_1), \xi_{\pm}^{kl}(\theta_2) \right) = \frac{(\sigma_e^i \sigma_e^j)^2}{N_p^{ij}(\theta_1)} \delta_{\theta_1 \theta_2}^K \left(\delta_{ik}^K \delta_{jl}^K + \delta_{il}^K \delta_{jk}^K \right), \quad (21)$$

where $N_p^{ij}(\theta)$ is as defined in Eq. (6). When boundary and masking effects are neglected, it can be approximated by

$$N_p^{ij}(\theta) = 2\pi A \theta \Delta_\theta \bar{n}_i \bar{n}_j, \quad (22)$$

385 where A is the survey area. On the other hand, a more accurate estimation of N_p^{ij} can be obtained by taking into account the survey mask, such that

$$N_p^{ij}(\theta) = 2\pi A \theta \Delta_\theta \bar{n}_i \bar{n}_j w_{\text{mask}}(\theta), \quad (23)$$

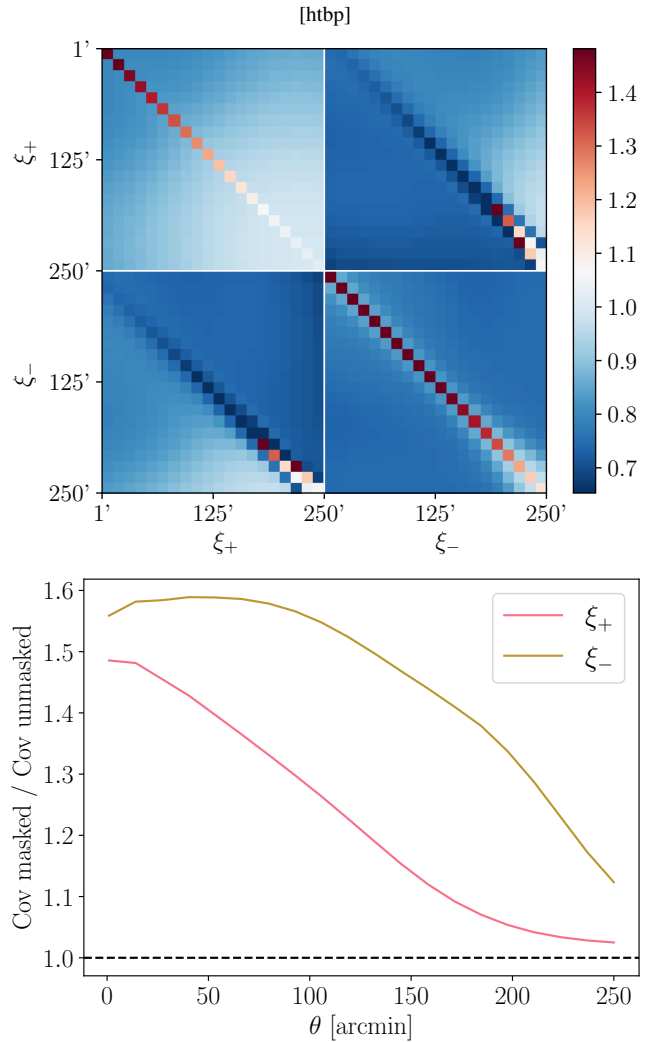


Figure 4. Ratio of the total covariance matrix with and without the survey mask, for both the auto-covariance and cross-covariance of the $\xi_{\pm}(\theta)$ correlation functions (top) and their diagonals (bottom), over $\theta = [1, 250]$ arcmin.

where the mask power spectrum $w_{\text{mask}}(\theta)$, normalised to the survey area, modifies N_p^{ij} .

We examine the effect of the UNIONS mask on the covariance matrix, and present the full ratio of the masked to unmasked covariance matrix, including the cross-covariances and non-Gaussian and SSC contributions, in Fig. 4. We find that overall, including masking effects increases the diagonal terms of the auto-covariance (i.e. the noise terms as defined in Eq. (21)), with a peak in the ratio occurring at approximately 1 arcmin for ξ_+ and 20 arcmin for ξ_- . This ratio decreases with increasing θ , as the angular separation of the measurement becomes larger than the masking scale. The overall impact of masking is larger for the uncertainties in ξ_- than ξ_+ . Our results are consistent with the trend and values found in Troxel et al. (2018), as shown in the bottom panel of their Fig. 1. On the other hand, the ratios of the off-diagonal and cross-covariance terms are reduced (except at large scales), since they receive a contribution coming from the SSC term. This is apparent in the integrand for σ_b^2 , where the survey window is rescaled by the mask power spectrum, thereby downweighting the contribution of modes suppressed by the survey mask to the overall background variance.

We adopt the masked covariance matrix as our fiducial, and also present results with the unmasked covariance to quantify its impact.

410 3.6 External data sets

Here we summarise the external data sets incorporated into our inference runs. These include highly complementary measurements from the CMB, which provide information at high redshifts, as well as BAO and Type Ia supernovae (SNeIa) data, which offer information on the expansion history at low redshifts. Combined with cosmic shear, they give a more complete description of the Universe at both the background and perturbation levels, tightening overall cosmological constraints.

3.6.1 Cosmic Microwave Background

The CMB, relic radiation from free-streaming photons that decoupled from baryons at redshifts $z \approx 1100$, provides highly precise constraints on early-Universe physics. We include data from the 2018 data release of the *Planck* mission (Planck Collaboration 2020a), specifically those of the *TT*, *TE* and *EE* auto- and cross-spectra, spanning a multipole range of $2 \leq \ell \leq 2508$ for *TT*, and $2 \leq \ell \leq 1996$ for *TE* and *EE*. To avoid having to sample over the large number of CMB nuisance parameters, we employ instead the *plik_lite* likelihood (Prince & Dunkley 2019), which assumes a Gaussian likelihood and only marginalises over A_{lens} , the correction amplitude due to lensing effects, as a nuisance parameter. Furthermore, we do not include the lensing power spectrum, as we currently lack a prescription for the cross-correlation in the covariance matrix between the cosmic shear and lensing data.

3.6.2 Baryonic Acoustic Oscillations

We include observations of the BAO scale from the second data release of the Dark Energy Spectroscopic Instrument (DESI DR2; Abdul Karim et al. 2025a,b), in the form of measurements of the transverse and comoving BAO distance (D_M and D_H respectively). They span a redshift range of $0.1 < z < 3$, and represent the most comprehensive and precise measurement of the BAO scale to date. The results attracted significant attention, as they favour a cosmological model with a varying dark energy equation of state over a cosmological constant Λ .

3.6.3 Type Ia Supernovae

Lastly, we consider data from SNeIa, which are model-independent standard candles that constrain the late-time distance-redshift relation. We employ the Pantheon+ data set (Brout et al. 2022), comprising observations of 1550 distinct SNeIa with a redshift range of $0.001 < z < 2.26$. Constraints on H_0 derived from SNeIa are famously in tension with those derived from early time CMB probes by approximately $2-4\sigma$ (Di Valentino et al. 2021). We combine BAO and SNeIa data, which together give information on the background expansion to constrain Ω_m and H_0 .

4 INFERENCE PIPELINE SETUP

We use Bayesian inference to derive constraints on the cosmological parameters of the concordance Λ CDM model from the data vectors, covariance matrix, and redshift distribution described above.

Bayesian inference relies on Bayes' Theorem, which gives the probability distribution of the parameters θ given a model M and the observed data d . This probability distribution $P(\theta|d, M)$, known as the posterior distribution, is defined as

$$P(\theta|d, M) = \frac{\mathcal{L}(d|\theta, M)\Pi(\theta|M)}{\mathcal{Z}(d|M)}, \quad (24)$$

where $\Pi(\theta|M)$ is the prior distribution, quantifying our initial knowledge of the distribution of θ , $\mathcal{Z}(d|M)$ is the evidence, which gives the probability of observing the data given M , and $\mathcal{L}(d|\theta, M)$ is known as the likelihood function, which is the probability of observing the data d given the model M with parameter values θ .

We adopt a Gaussian likelihood:

$$-2 \log \mathcal{L} \propto [d - T(\theta)]^T \mathbf{C}^{-1} [d - T(\theta)], \quad (25)$$

where d is the data vector, $T(\theta)$ is the theory vector derived from the model, and \mathbf{C} is the covariance matrix of the data, assumed to be Gaussian.

4.1 Likelihood inference

We use the Einstein–Boltzmann solver *CAMB* (Lewis et al. 2000) to calculate cosmological quantities and the linear matter power spectrum, and the *CosmoSIS* (Zuntz et al. 2015) pipeline for parameter inference. Our baseline sampler is *Polychord* (Handley et al. 2015a,b), following many other Stage III survey analyses (Abbott et al. 2022; Dalal et al. 2023; Li et al. 2023a; Anbjagane et al. 2025). *Polychord* produces reliable posterior estimates at reasonable computational cost (Lemos et al. 2023), though it becomes expensive as the parameter space grows. We therefore also run *Nautilus* (Lange 2023), which uses deep learning to improve efficiency (Wright et al. 2025a; Euclid Collaboration: Cañas-Herrera et al. 2025), as a sampler consistency check.

In terms of prior ranges for the cosmological parameters, we adopt those given in table 2 of Abbott et al. (2023), except that we additionally impose a prior on the baryonic energy density parameter $\omega_b \equiv \Omega_b h^2$ derived from Big Bang nucleosynthesis (BBN) constraints, computed with the *PRyModial* code (Burns et al. 2024; Schöneberg 2024), which gives $\omega_b = 0.02218 \pm 0.00055$ assuming a Λ CDM model. In total, the cosmological parameters being sampled are $\{\omega_c, \omega_b, H_0, n_s, S_8\}$: the energy density of cold dark matter; the energy density of baryons; the present-day value of the Hubble parameter; the spectral index; and the amplitude of clustering $S_8 \equiv \sigma_8 \sqrt{\Omega_m/0.3}$ ¹. Since the optical depth of reionisation τ_{reio} is not well constrained with cosmic shear data, we fix it at the *Planck* 2018 best-fit value of $\tau_{\text{reio}} = 0.0544$ (Planck Collaboration 2020b). However, when including CMB data, we do not impose the BBN prior, and additionally sample τ_{reio} . We also assume a flat Universe and one massive and two massless neutrino species, with a total mass of $\Sigma m_\nu = 0.06\text{eV}$. The following subsections describe the modelling of intrinsic alignment, the nonlinear matter power spectrum, and PSF leakage. Table 2 lists the full set of priors for the cosmological and nuisance parameters that we sample in our analysis.

¹ Joachimi et al. (2021) argued that sampling S_8 gives a more uninformative prior volume as opposed to sampling A_s , the amplitude of the primordial power spectrum. This methodology has since been adopted in Asgari et al. (2021); Wright et al. (2025a).

4.2 Intrinsic alignment

Multiple strategies to disentangle intrinsic alignment (IA) from cosmic shear require accurate estimates of galaxy redshifts (Joachimi & Schneider 2010). Recent cosmic shear measurements have been somewhat successful in directly estimating the intrinsic alignment parameters when jointly fitting the shear-shear ($\gamma\gamma$), shear-intrinsic (γI) and intrinsic-intrinsic (II) correlations to the signal (Asgari et al. 2021; Secco et al. 2022). This success can be traced back to the very different ways these effects act with respect to galaxy separation: small angular bins are more affected by II contributions, while bins with larger separation have a strong γI contribution.

In Fourier space, the noiseless cosmic shear angular power spectrum decomposes as

$$C_\ell^{\epsilon\epsilon} = C_\ell^{\gamma\gamma} + C_\ell^{\gamma I} + C_\ell^{II}. \quad (26)$$

Models exist which give an approximate theoretical prescription for the latter two terms, with one of the widely employed models being the redshift-dependent nonlinear alignment model (NLA; Hirata & Seljak 2004; Bridle & King 2007). Here, the 3D power spectra $P^{\gamma I}(k, z)$ and $P^{II}(k, z)$ are expressed as a rescaling of the nonlinear matter power spectrum

$$P^{\gamma I}(k, z) = -A_{IA} C_1 \rho_{\text{crit}} \frac{\Omega_m}{D(z)} P_{\text{NL}}(k, z), \quad (27)$$

$$P^{II}(k, z) = \left(A_{IA} C_1 \rho_{\text{crit}} \frac{\Omega_m}{D(z)} \right)^2 P_{\text{NL}}(k, z), \quad (28)$$

where A_{IA} is a dimensionless IA amplitude parameter to be marginalised over, ρ_{crit} is the critical energy density, $D(z)$ is the growth factor and $C_1 = 5 \times 10^{-14} h^{-2} M_{\odot}^{-1} \text{Mpc}^3$.

In this analysis, the use of a single redshift bin prohibits us from efficiently constraining A_{IA} , necessitating the imposition of a well-motivated prior. Since multiple direct intrinsic alignment measurement models have been proposed (Joachimi et al. 2011; Mandelbaum et al. 2011; Singh et al. 2015; Johnston et al. 2019; Fortuna et al. 2021b; Samuroff et al. 2023; Hervas Peters et al. 2025; Navarro-Gironés et al. 2025), we choose to rely on these, further ignoring the impact of any higher-order terms, such as those proposed in the tidal alignment tidal torquing model (TATT; Blazek et al. 2019). This strategy has also been adopted in previous works (Fortuna et al. 2021a; Li et al. 2023c; Wright et al. 2025a).

We use a data-driven approach to estimate A_{IA} , making use of the same W3 CFHTLenS BPZ (Benítez 2000) catalogue from which the $n(z)$ was derived. We then adopt the commonly employed method of splitting intrinsic alignment contributions coming from red and blue galaxies (Krause et al. 2016), motivated by the distinction between pressure-supported and rotationally supported galaxies, respectively. The parametrisation is given by

$$A_{IA} = f_r A_{IA,r} + f_b A_{IA,b}. \quad (29)$$

where f_r indicates the fraction of red galaxies, and f_b indicates the fraction of blue galaxies within our sample. For simplicity, we do not introduce any luminosity or redshift dependence, hence A_{IA} is a constant parameter. To separate blue from red galaxies, we choose to assign all galaxies with $T_B < 1.9$ as red galaxies and treat the rest as blue. The determination of the T_B index is done through BPZ, where it utilises six model templates, arranged by increasing star formation activity, and performs linear interpolation between neighbouring templates to find the best-matching spectral energy distribution. The output parameter, T_B , represents the selected best-fit template, or more precisely the blend of adjacent templates, in steps of 0.1. From there, we obtain estimates for $f_r = 0.245$ and $f_b = 0.745$.

For the values $A_{IA,r}$ and $A_{IA,b}$, we use prior values derived from direct measurements. These rely on accurate redshift estimation, either photometric or spectroscopic, to compute the projected shape-density correlation function w_{g+} with limited separation. For the blue galaxy sample, we adopt the result from Johnston et al. (2019), which fitted the available measurements to obtain $A_{IA,b} = 0.21 \pm 0.37$. While other works using this model have set the intrinsic alignment of blue galaxies to 0 (consistent with the data), we prefer a more conservative approach and adopt this observationally grounded prior with a non-negligible Gaussian width. For an estimate of $A_{IA,r}$, we sample from the posterior distribution of the double power-law fit done on $A_{IA}(L/L_0)$, at the mean luminosity value of red galaxies measured on W3. The luminosities are obtained from LePhare (Arnouts & Ilbert 2011), where the mean value for UNIONS is found to be $(L/L_0) = -0.77$. Sampling the posterior gives us $A_{IA,r} = 2.75 \pm 0.49$, a value in accordance with most KiDS estimates, but not with fiducial DES values (Abbott et al. 2023). We then add the Gaussian errors in quadrature to arrive at a prior of $A_{IA} = 0.83 \pm 0.39$. We have tested the robustness of this prior against changes in T_B , finding only small differences.

This method is mainly limited by two factors. First, the galaxies for which reliable spectroscopic or photometric redshifts are available are not representative of either the blue or red population, since they mostly need to be bright to have reliable photometric redshifts or be targeted by spectroscopic surveys. Second, these various methods are all obtained with different lensing surveys. It has been shown that the shape algorithm used (Singh & Mandelbaum 2016) and the band the galaxy has been measured in Georgiou et al. (2019) impact the measured amplitude of the intrinsic alignment signal. These two reasons motivate the doubling of the width of our Gaussian prior to ± 0.78 instead. For comparison, we also conduct a run assuming an uninformative flat prior on A_{IA} .

4.3 PSF leakage

To mitigate systematic effects from PSF leakage, we employ two safeguards: firstly, we apply scale cuts to ensure that the additive contribution from the leakage signal, $\xi_{\pm}^{\text{PSF,sys}}$, remains below 10% of the total measured signal. Additionally, we have chosen to jointly fit the observed correlation function signal ξ_{\pm}^{obs} with the τ statistics as introduced in Sect. 3.2.1. Specifically, we sample α and β as nuisance parameters and compute the theoretical τ statistics according to Eq. (10), given the $\rho(\theta)$'s estimated from the data. Since we set $\eta = 0$, this would require only the computation of $\tau_0(\theta)$ and $\tau_2(\theta)$, where we only consider the τ_+ signal. The τ statistic likelihood is thus calculated as

$$\chi_{\tau_{0,2}}^2 = [\tau_{0,2,d}(\theta) - \tau_{0,2,t}(\theta)]^T \mathbf{C}_{\tau}^{-1} [\tau_{0,2,d}(\theta) - \tau_{0,2,t}(\theta)], \quad (30)$$

where the subscripts ‘d’ and ‘t’ denote the data and theory vectors respectively. \mathbf{C}_{τ} is a semi-analytical covariance, presented in Fig. 3 concatenated with the shear-shear covariance; see Guerrini et al. (2025) for its full derivation. Cross-correlations between the shear-shear 2PCF and the τ statistics are neglected for simplicity.

Additionally, we include the PSF leakage contribution as an additive bias to the cosmological signal, by calculating the theoretical ξ_{\pm}^{sys} following Eq. (11), given the sampled values of α and β . The total log-likelihood being minimised is thus

$$\chi_{\text{tot}}^2 = \chi_{\xi_{\pm}^{\text{obs}}}^2 + \chi_{\xi_{\pm}^{\text{obs}}}^2 + \chi_{\tau_0}^2 + \chi_{\tau_2}^2. \quad (31)$$

This joint fit accounts for the additive leakage bias and marginalises over PSF systematic uncertainty. Other Stage III surveys employ a similar approach (see for example Li et al. 2023a; Zhang et al. 2023).

Table 2. Sampled cosmological and nuisance parameters with their adopted priors. Uniform and Gaussian priors are listed in the table, with CMB-specific ranges indicated where relevant.

Parameter	Prior
Cosmology	
ω_b [no CMB]	$\mathcal{N}(0.02218, 0.00055)$
ω_b [with CMB]	$\mathcal{U}(0.019, 0.026)$
ω_c	$\mathcal{U}(0.051, 0.255)$
h	$\mathcal{U}(0.64, 0.82)$
n_s	$\mathcal{U}(0.84, 1.1)$
S_8	$\mathcal{U}(0.1, 1.3)$
$\log_{10}(T_{\text{AGN}}/\text{K})$	$\mathcal{U}(7.3, 8.0)$
τ_{reio} [with CMB]	$\mathcal{U}(0.01, 0.8)$
Nuisance	
A_{IA}	$\mathcal{N}(0.83, 0.78)$
α_{PSF} (leakage corrected)	$\mathcal{N}(0.0050, 0.0021)$
β_{PSF} (leakage corrected)	$\mathcal{N}(0.8065, 0.1127)$
α_{PSF} (non-leakage corrected)	$\mathcal{N}(0.0222, 0.026)$
β_{PSF} (non-leakage corrected)	$\mathcal{N}(0.7696, 0.1120)$
Δz	$\mathcal{N}(0.033, 0.013)$
m	$\mathcal{U}()$

For the fiducial analysis, we use Gaussian priors on α and β rather than flat priors. For data vectors with significant PSF leakage, unconstrained α and β risk biased posteriors. Specifically, if these parameters are left unconstrained (i.e., with wide priors) during the main cosmological inference step, they may fit the cosmological signal ξ_{\pm}^{yy} rather than the systematic ξ_{\pm}^{sys} (Eq. (12)), since non-trivial degeneracies exist between leakage and cosmological parameters. Consequently, the resulting posteriors on α and β would be inconsistent with those from a direct ρ/τ fit.

To obtain the priors on α and β , we first run a separate ‘PSF leakage inference step’ whereby we solely fit α and β based on the ρ and τ statistics estimated from the data, per Eq. (10). This is the methodology described above. We use a vanilla emcee sampler to minimise $\chi^2_{\tau_{0.2}}$, and the resulting posteriors of α and β serve as priors in the cosmological inference step (see Table 2 for their values). We refer the reader to Guerrini et al. (2025) for a detailed description of the methodology of this PSF leakage inference step.

We also conduct a PSF inference run where we use the catalogue containing the set of galaxy ellipticities that have not been corrected for PSF leakage, i.e., not corrected object-wise (see Paper I for details). These ellipticities give different values of $\tau(\theta)$, $\rho(\theta)$, and subsequently different posteriors for α and β . Figure 5 shows the marginalised posteriors of α and β for both the object-wise leakage-corrected and uncorrected ellipticities. The non-leakage-corrected case (in pink) shows a larger mean α , as expected from the greater residual PSF leakage when the object-wise correction is not applied. On the other hand, β remains largely constant, showing that the object-wise correction mainly accounts for the PSF model ellipticity, e^p . Nonetheless, leakage not corrected at the object level can be absorbed into a larger α , and thus a larger $\xi_{\pm}^{\text{PSF,sys}}$, giving consistent cosmological posteriors with the leakage-corrected case.

For comparison, we also conduct a cosmological inference run where we instead adopt flat priors on α and β , to assess the impact of the PSF inference step on the additive leakage bias estimate $\xi_{\pm}^{\text{PSF,sys}}$.

4.4 Redshift calibration bias estimation

Biases in the spectroscopic calibration of the redshift distribution $n(z)$ propagate into cosmological parameter inference. We therefore

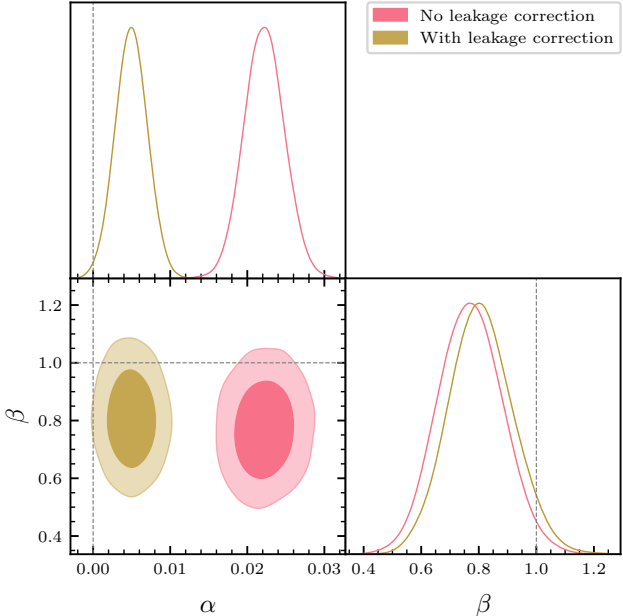


Figure 5. Marginalised posteriors of α_{PSF} and β_{PSF} obtained from the PSF inference step (see Sect. 4.3), which are subsequently adopted as priors when they are sampled in the cosmological inference analysis. We include the results for both sets of ellipticities: the object-wise leakage corrected one (gold) and the non-leakage corrected one (pink). The catalogue-level object-wise leakage correction effectively removes the leakage component of the additive bias (α is close to 0 for the gold contours).

marginalise over Δz , the bias in the mean redshift. Here we describe how we obtain an informed prior on this parameter.

Because the true $n(z)$ of the data is unknown, this bias can only be assessed using simulations, where the true redshifts are available. By constructing mock catalogues that mimic the photometric properties, selection functions, and redshift-calibration steps of the real UNIONS analysis, we directly compare the recovered SOM-based $n(z)$ to the true underlying distribution, obtaining estimates of the systematic shift Δz .

We construct our mock catalogues from the MICE2 galaxy catalogue, generated from the MICE Λ CDM cosmology and evolves a large-volume dark-matter distribution with sufficient resolution for weak-lensing applications. Dark-matter haloes are identified using a friends-of-friends algorithm (Crocce et al. 2015), and galaxies are populated up to $z = 1.4$ through a hybrid scheme combining halo abundance matching with a halo occupation distribution model, calibrated to reproduce the observed luminosity function and galaxy clustering (Carretero et al. 2015). To account for empirical luminosity evolution, we apply the redshift-dependent magnitude-evolution correction of Fosalba et al. (2015a).

To perform the same redshift calibration analysis as in the real UNIONS data, we require that the MICE2 galaxies have realistic multi-band photometry. In the observational data, the UNIONS r -band sources are matched to CFHTLenS to obtain five-band $ugriz$ magnitudes (Hildebrandt et al. 2012), which are used for the SOM-based redshift calibration. For the mock catalogues, we therefore replicate this photometric setup by generating CFHTLenS-like noisy fluxes for every simulated galaxy. We adopt a noise-modelling framework inspired by van den Busch et al. (2020), adapted to the depth and filter properties of the CFHTLenS imaging (Erben et al. 2013).

Through this procedure, we obtain noisy fluxes depending on galaxy size, seeing variations and the intrinsic brightness of each source.

In a further step, we employ a kNN-based matching procedure following the approach presented in Wright et al. (2025b) to ensure that the simulated catalogues replicate the photometric and spectroscopic selection functions of the UNIONS analysis. The UNIONS weak-lensing sample is matched to deeper CFHTLenS *ugriz* photometry in the W3 field. To reproduce this in the mocks, we match the noisy MICE2 galaxies to the real UNIONS–CFHTLenS sources using kNN-matching in colour–magnitude space. For each real galaxy, we select the nearest simulated object (conditioning on similar true redshift) and transfer its multi-band properties to construct a photometric sample that follows the joint distributions of colour, magnitude, S/N and size observed in the data. We also transfer the shape weights w^{shape} and the shear-response weights w^R from the real UNIONS shear catalogue to the simulations, since we need these in the SOM-based redshift calibration (as described in Sect. 3.3).

To replicate the spectroscopic calibration set consisting of DEEP2, VVDS, and VIPERS, we create a second mock sample using kNN-matching between these surveys and the noisy MICE2 galaxies. Matching in colour–magnitude space ensures that the mock calibration sample follows the same selection function as the combined real spectroscopic data set.

The mock photometric and spectroscopic samples are processed using the same SOM-based redshift calibration pipeline employed for the real UNIONS data (Sect. 3.3). The SOM is trained on the spectroscopic-like mock sample, and the photometric mocks are projected onto the trained map to yield a recovered $n(z)$, weighted by both the shape and shear response weights. From the jackknife resampling, we recover a redshift distribution, which we compare to the true redshift distribution of the simulated sources. This provides a direct measure of the redshift-calibration bias, which we find to be $\Delta z = 0.033$.

The width of the prior on Δz is derived directly from the data: we use the standard deviation of the jackknife realisations of the SOM-based $n(z)$ obtained by resampling the spectroscopic calibration sample. This jackknife-based estimate of the uncertainty is fully data-driven, and we verified with the mock catalogues that it is consistent with the scatter expected from the true redshift-calibration error budget. We therefore estimate the uncertainty to be ± 0.013 .

4.5 Nonlinear matter power spectrum

Cosmic shear probes small scales of the matter power spectrum, requiring accurate modelling of the nonlinear regime. Following the methodology of Doux et al. (2021), we derive the contribution of each wavenumber k of the nonlinear matter power spectrum to the 2PCF signal at different angular scales by calculating the integral given in Eq. (2). We adopt the *Planck* 2018 best-fit cosmology (Planck Collaboration 2020b) as our fiducial model, and employ the Limber approximation to convert $k_{\max} = (\ell + 1/2)/\chi(z_{\min})$, where $\chi(z)$ is the radial comoving distance. Figure 6 presents a heatmap of the ratio of the total 2PCF signal as a function of k and θ scale, for both ξ_+ and ξ_- . With the conservative criterion that scales beyond $k_{\max} = 3 h \text{ Mpc}^{-1}$ contribute less than 10% of the signal, our $n(z)$ implies minimum angular scales of 1.5 arcmin for ξ_+ and 11 arcmin for ξ_- . However, as described in Sect. 4.6, by considering the effects of B -mode contamination, we instead adopt a fiducial angular lower bound of $\theta = 12 \text{ arcmin}$, which would then imply that scales beyond $k_{\max} = 0.39 h \text{ Mpc}^{-1}$ do not contribute to more than 10% of the $\xi_+(\theta)$ signal, and scales beyond $k_{\max} = 2.75 h \text{ Mpc}^{-1}$ for the $\xi_-(\theta)$ signal. These scale cuts are safely within the range of accuracy of the

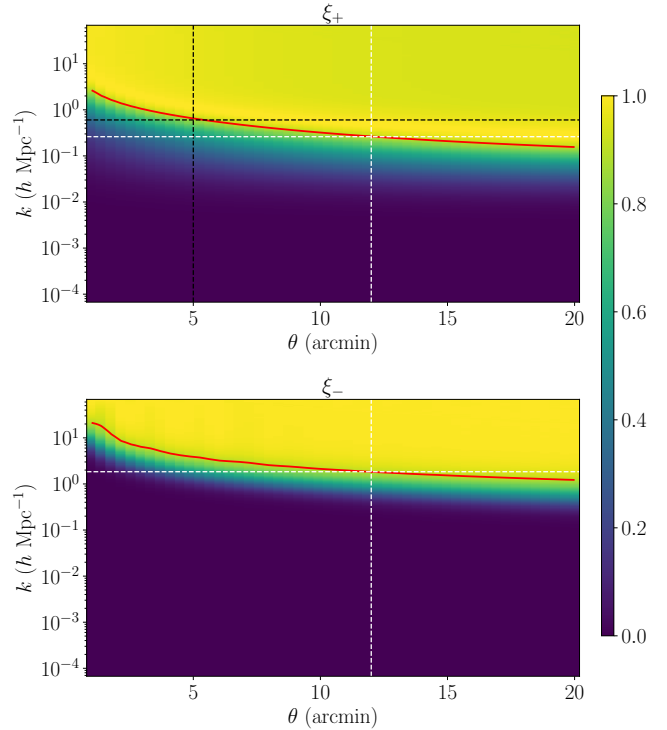


Figure 6. Ratio of the 2PCF signal as a function of k scale, for different values of angular separation θ (ξ_+ , upper; ξ_- , lower). The red contour marks the boundary at which k_{\max} scales contribute 90% of the signal. White dashed lines mark the fiducial scale cuts: a 12 arcmin lower bound for ξ_+ corresponds to $k_{\max} = 0.39 h \text{ Mpc}^{-1}$, and $k_{\max} = 2.75 h \text{ Mpc}^{-1}$ for ξ_- . Black lines mark the 5 arcmin lower scale cut explored in one inference run (Sect. 4.6).

nonlinear prescriptions adopted below. We mark out these boundaries in Fig. 6 as well.

For our fiducial analysis, we use the most updated version of HMCode2020 (Mead et al. 2021), which employs the halo model formalism as well as baryonic feedback modelling to calculate the nonlinear matter power spectrum, with up to 2.5% accuracy at scales $k \leq 10 h \text{ Mpc}^{-1}$ when compared to N -body simulations. It has also been widely adopted in other Stage III cosmic shear analyses (Hikage et al. 2019; Gatti et al. 2021; Wright et al. 2025a).

When modelling the small-scale baryonic feedback arising from active galactic nuclei (AGN), an additional parameter $\log(T_{\text{AGN}})$ is introduced, which quantifies the ‘temperature’ or strength of this feedback. Calibrations with N -body simulations estimate it to be around 7.6–8.0. In our fiducial analysis, we marginalise over this parameter, while also including a test where we do not account for baryonic feedback to quantify its impact on the clustering cosmological parameters σ_8 and S_8 . We also run a test without baryonic feedback (disabling the ‘feedback’ option in HMCode2020) and one using the nonlinear prescription of Halofit (Takahashi et al. 2012) instead, which is based on a halo-fitting model, to quantify the sensitivity of our data to a difference in nonlinear modelling.

4.6 Scale cuts

Our null-test-motivated baseline scale cuts are determined by three criteria: PSF leakage, B -mode analyses, and potential mismodelling of the nonlinear power spectrum at small scales, described in Sects. 3.2.1, 3.2.2, and 4.5, respectively. By setting the require-

ments that the real space and COSEBIs B -mode null tests are passed with a PTE of at least 0.05, and that the PSF leakage signal $\xi_{\pm}^{\text{PSF,sys}}$ does not contribute more than 10% of the total signal, we obtain
770 $\theta = [5, 83]$ arcmin for ξ_+ and $\theta = [12, 83]$ for ξ_- .

To assess the sensitivity of our scale cut choices to cosmology, we conducted blinded inference analyses by successively increasing the values of the lower scale cut of ξ_+ , with θ_{\min} varying from 3.98 to 12.0 arcmin. The results showed a nontrivial S_8 dependence on scale,
775 with a systematic downward drift in S_8 and an improved χ^2 value with increasing θ_{\min} . We therefore remove angular bins where the induced shift in the mean S_8 exceeds 0.2σ . This behaviour eventually stabilises, going from the ninth to the tenth angular bin (representing a θ_{\min} increase from 9.10 arcmin to 12.0 arcmin), where we also find the largest χ^2 improvement of 0.7. This could be correlated with the exclusion of the localised feature around 10 arcmin of the ξ_+ function
780 (see Fig. 1), coincident with the 9.4 arcmin size of the MegaCam CCD. This feature persisted with similar amplitude across different variations of PSF size cuts and masking schemes, appearing in both the cosmological and systematic ξ_+^B signals. Additionally, we found that scale cut combinations of $\theta = [5, 83]$ and $\theta = [12, 83]$ pass the COSEBIs B -mode null test, but not for the case of $\theta = [9, 12]$ (see Paper III for details). The fiducial scale cut is therefore $\theta = [12, 83]$ arcmin for ξ_+ . However, for completeness, we also present inference results where we allow for small-scale contributions in ξ_+ ,
790 i.e. when $\theta = [5, 83]$ arcmin.

4.7 Pipeline validation with mock catalogues

With our inference pipeline set up, we validate it by running it on 350 random galaxy mock catalogues generated using GLASS (Tessore et al. 2023). The catalogues were created with the same mask, effective number density and σ_e as the data, with a *Planck* 2018 best-fit fiducial cosmology. In addition, one of the blinded $n(z)$ distributions was chosen at random. We refer the reader to Appendix A for a validation of the mock galaxy survey properties. The mock catalogues
800 contain no PSF systematics, so the τ statistics are consistent with zero. We nonetheless account for PSF leakage uncertainty by sampling α and β with priors obtained from the ρ and τ statistics of the mock data vectors. Both parameters recover a zero mean to within 1 σ .

We measure the cosmic shear and PSF correlation functions, compute the masked covariance matrix, and run inference on each mock catalogue, employing the parameters and priors as in Table 2 and the same fiducial scale cuts as detailed in Sect. 4.6. This test acts as a criterion for unblinding (see Sect. 4.8). First, we assess whether we recover the fiducial cosmology within a reasonable level of uncertainty. Additionally, we run our pipelines on the same set of mocks using both the configuration and Fourier space pipelines to check that the average S_8 mean obtained from both analyses differ by less than 1 σ .

4.8 Blinding Strategy

We conduct a blinded analysis to remain agnostic to the results and prevent confirmation biases when making analysis choices. Blinding was performed by an external collaborator who applied a random shift to the $n(z)$ distribution, thus inducing an offset in the marginalised S_8 posterior distributions (Eqs. (3) and (4)). Three versions of the $n(z)$ were generated, one of which was not shifted. We then computed the covariance matrices and performed the cosmological inference for all three $n(z)$ distributions. Because the data vector itself was

not blinded, we were able to directly employ the tests described in Sect. 3.2 as a diagnostic of systematic contamination. The covariance matrix used to calculate the PTEs changes with each $n(z)$ shift, but we have verified that the percentage difference between each of them are below 10%, and the resulting PTE variations do not affect our conclusions about unblinding or scale cuts. We calculate PTEs using all three covariances and take the most conservative value.
825

The bulk of this manuscript was prepared prior to unblinding and underwent review by the broader UNIONS collaboration, including the external blinding coordinator. As detailed in the previous section, before proceeding to unblind, we ran both the Fourier and configuration space pipelines on 350 mock galaxy catalogues each (Sect. 4.7). From the histogram of the recovered mean values of Ω_m and σ_8 in Fig. A2, we recover the fiducial cosmology to within 1 σ . From Fig. A3, we find consistent S_8 means for both configuration and Fourier space analyses, with $\Delta\langle S_8 \rangle = 0$ within 1 σ . We also assess the sensitivity of our blinded data vectors to systematic effects, such as inclusion of the PSF additive bias ξ_{sys} , scale cuts, and differences in nonlinear modelling. We verified that the differences in the posteriors due to these analysis choices are consistent throughout the three blinds (as presented in Fig. A4). The analysis pipeline is robust to these choices. We present the unblinded results in the following section.
835
840
845

5 RESULTS

5.1 Fiducial analysis

5.2 Robustness to modelling choices

5.2.1 Scale cuts

5.2.2 Systematics

5.2.3 Sampler

5.2.4 Nonlinear matter power spectrum modelling

5.3 Comparison to external data sets

5.3.1 CMB

5.3.2 CMB + BAO + SNeIa

6 CONCLUSION

ACKNOWLEDGEMENTS

We would like to thank our external blinding coordinator, Koen Kuijken. LWKG thanks the University of Edinburgh School of Physics and Astronomy for a postdoctoral Fellowship. HH is supported by a DFG Heisenberg grant (Hi 1495/5-1), the DFG Collaborative Research Center SFB1491, an ERC Consolidator Grant (No. 770935), and the DLR project 50QE2305. MJH and LVW acknowledge support from NSERC through a Discovery Grant. This work was made possible by utilising the CANDIDE cluster at the Institut d’Astrophysique de Paris. The cluster was funded through grants from the PNCG, CNES, DIM-ACAV, the Euclid Consortium, and the Danish National Research Foundation Cosmic Dawn Center (DNRF140). The authors acknowledge the use of the Canadian Advanced Network for Astronomy Research (CANFAR) Science Platform operated by the Canadian Astronomy Data Centre (CADC) and the Digital Research Alliance of Canada (DRAC), with support from the National Research Council of Canada (NRC), the Canadian Space Agency (CSA), CANARIE, and the Canada Foundation for Innovation (CFI). It is maintained by Stephane Rouberol. We are honoured and grateful
850
855
860
865
870
875
880
885
890
895
900
905
910
915
920
925
930
935

for the opportunity of observing the Universe from Maunakea and Haleakala, which both have cultural, historical and natural significance in Hawaii. This work is based on data obtained as part of the Canada-France Imaging Survey, a CFHT large program of the National Research Council of Canada and the French Centre National de la Recherche Scientifique. Based on observations obtained with MegaPrime/MegaCam, a joint project of CFHT and CEA Saclay, at the Canada-France-Hawaii Telescope (CFHT) which is operated by the National Research Council (NRC) of Canada, the Institut National des Science de l'Univers (INSU) of the Centre National de la Recherche Scientifique (CNRS) of France, and the University of Hawaii. This research is based in part on data collected at Subaru Telescope, which is operated by the National Astronomical Observatory of Japan. Pan-STARRS is a project of the Institute for Astronomy of the University of Hawaii, and is supported by the NASA SSO Near Earth Observation Program under grants 80NSSC18K0971, NNX14AM74G, NNX12AR65G, NNX13AQ47G, NNX08AR22G, 80NSSC21K1572 and by the State of Hawaii.

895 DATA AVAILABILITY

A subset of the raw data underlying this article is publicly available via the Canadian Astronomical Data Centre at <http://www.cadc-ccda.hia-ihc.nrc-cnrc.gc.ca/en/megapipe/>. The remaining raw data and all processed data are available to members of the Canadian and French communities via reasonable requests to the principal investigators of the Canada-France Imaging Survey, Alan McConnachie and Jean-Charles Cuillandre. All inference chains and software used to produce the results will be publicly available to the international community upon paper acceptance.

905 REFERENCES

- Abbott T. M. C., et al., 2022, *Phys. Rev. D*, 105, 023520
 Abbott T. M. C., et al., 2023, *Open J. Astrophys.*, 6, 2305.17173
 Abdul Karim M., et al., 2025a, *Phys. Rev. D*, 112, 083514
 Abdul Karim M., et al., 2025b, *Phys. Rev. D*, 112, 083515
 Albrecht A., et al., 2006, *arXiv e-prints*, pp astro-ph/0609591
 Anbabagane D., et al., 2025, *Open J. Astrophys.*, 8, 146161
 Arnouts S., Ilbert O., 2011, LePHARE: Photometric Analysis for Redshift Estimate, Astrophysics Source Code Library, record ascl:1108.009
 Asgari M., Schneider P., Simon P., 2012, *A&A*, 542, A122
 Asgari M., et al., 2021, *A&A*, 645, A104
 Bacon D. J., Refregier A. R., Ellis R. S., 2000, *MNRAS*, 318, 625
 Bartelmann M., Schneider P., 2001, *Phys. Rept.*, 340, 291
 Bechtol K., et al., 2025, *arXiv e-prints*, p. arXiv:2501.05739
 Benítez N., 2000, *ApJ*, 536, 571
 Bertin E., 2011, in Evans I. N., Accomazzi A., Mink D. J., Rots A. H., eds, Astronomical Society of the Pacific Conference Series Vol. 442, Astronomical Data Analysis Software and Systems XX. p. 435
 Blazek J. A., MacCrann N., Troxel M., Fang X., 2019, *Phys. Rev. D*, 100, 103506
 Bridle S., King L., 2007, *New Journal of Physics*, 9, 444
 Brout D., et al., 2022, *ApJ*, 938, 110
 Burns A.-K., Tait T. M. P., Valli M., 2024, *European Physical Journal C*, 84, 86
 Carretero J., Castander F. J., Gaztanaga E., Crocce M., Fosalba P., 2015, *MNRAS*, 447, 646
 Choppin de Janvry J., Dai B., Gontcho S. G. A., Seljak U., Zhang T., 2025, *arXiv e-prints*, p. arXiv:2511.18134
 Cooray A., Sheth R. K., 2002, *Phys. Rept.*, 372, 1
 Crocce M., Castander F. J., Gaztanaga E., Fosalba P., Carretero J., 2015, *MNRAS*, 453, 1513
 Dalal R., et al., 2023, *Phys. Rev. D*, 108, 123519
 Daley C., et al., 2026, in preparation
 Di Valentino E., et al., 2021, *Classical and Quantum Gravity*, 38, 153001
 Di Valentino E., et al., 2025, *Physics of the Dark Universe*, 49, 101965
 Doux C., et al., 2021, *MNRAS*, 503, 3796
 Erben T., et al., 2013, *MNRAS*, 433, 2545
 Euclid Collaboration: Cañas-Herrera G., et al., 2025, *arXiv e-prints*, p. arXiv:2510.09153
 Euclid Collaboration: Mellier Y., et al., 2025, *A&A*, 697, A1
 Fang X., Eifler T., Krause E., 2020, *MNRAS*, 497, 2699–2714
 Farrens S., et al., 2022, *A&A*, 664, A141
 Fortuna M. C., Hoekstra H., Joachimi B., Johnston H., Chisari N. E., Georgiou C., Mahony C., 2021a, *MNRAS*, 501, 2983
 Fortuna M. C., et al., 2021b, *A&A*, 654, A76
 Fosalba P., Gaztanaga E., Castander F. J., Crocce M., 2015a, *MNRAS*, 447, 1319
 Fosalba P., Crocce M., Gaztanaga E., Castander F. J., 2015b, *MNRAS*, 448, 2987
 Friedrich O., et al., 2021, *MNRAS*, 508, 3125
 Gatti M., et al., 2021, *MNRAS*, 504, 4312–4336
 Georgiou C., et al., 2019, *A&A*, 622, A90
 Giblin B., et al., 2021, *A&A*, 645, A105
 Guerrini S., et al., 2025, *A&A*, 700, A215
 Guerrini S., et al., 2026, in preparation
 Guinot A., et al., 2022, *A&A*, 666, A162
 Gwyn S., et al., 2025, *AJ*, 170, 324
 Hamana T., et al., 2020, *PASJ*, 72, 16
 Handley W., Hobson M. P., Lasenby A. N., 2015a, *MNRAS*, 450, L61
 Handley W., Hobson M. P., Lasenby A. N., 2015b, *MNRAS*, 453, 4384
 Hervás Peters F., et al., 2025, *A&A*, 699, A201
 Hervás Peters F., et al., 2026a, in preparation
 Hervás Peters F., et al., 2026b, in preparation
 Heymans C., et al., 2012, *MNRAS*, 427, 146
 Hikage C., et al., 2019, *PASJ*, 71, 43
 Hildebrandt H., et al., 2012, *MNRAS*, 421, 2355
 Hirata C. M., Seljak U., 2004, *Phys. Rev. D*, 70, 063526
 Hu W., Jain B., 2004, *Phys. Rev. D*, 70, 043009
 Huff E., Mandelbaum R., 2017, *arXiv e-prints*
 Ivezić Ž., et al., 2019, *ApJ*, 873, 111
 Jarvis M., Bernstein G., Jain B., 2004, *MNRAS*, 352, 338
 Jarvis M., et al., 2016, *MNRAS*, 460, 2245
 Joachimi B., Schneider P., 2010, *arXiv e-prints*, p. arXiv:1009.2024
 Joachimi B., Mandelbaum R., Abdalla F. B., Bridle S. L., 2011, *A&A*, 527, A26
 Joachimi B., et al., 2021, *A&A*, 646, A129
 Johnston H., et al., 2019, *A&A*, 624, A30
 Kaiser N., 1992, *ApJ*, 388, 272
 Kaiser N., 1998, *ApJ*, 498, 26
 Kaiser N., Wilson G., Luppino G. A., 2000, *arXiv e-prints*, pp astro-ph/0003338
 Kilbinger M., 2015, *Rept. Prog. Phys.*, 78, 086901
 Kohonen T., 1982, Biological cybernetics, 43, 59
 Krause E., Eifler T., 2017, *MNRAS*, 470, 2100
 Krause E., Eifler T., Blazek J., 2016, *MNRAS*, 456, 207
 Lacasa F., Rosenfeld R., 2016, *JCAP*, 2016, 005–005
 Lange J. U., 2023, *MNRAS*, 525, 3181
 Le Fèvre O., et al., 2005, *A&A*, 439, 845
 Lemos P., et al., 2023, *MNRAS*, 521, 1184
 Lewis A., Challinor A., Lasenby A., 2000, *ApJ*, 538, 473
 Li X., et al., 2022, *PASJ*, 74, 421
 Li X., et al., 2023a, *Phys. Rev. D*, 108, 123518
 Li S.-S., et al., 2023b, *A&A*, 670, A100
 Li S.-S., et al., 2023c, *A&A*, 679, A133
 Mandelbaum R., et al., 2011, *MNRAS*, 410, 844
 Masters D., et al., 2015, *ApJ*, 813, 53
 Mead A. J., Brieden S., Tröster T., Heymans C., 2021, *MNRAS*, 502, 1401
 Myles J., et al., 2021, *MNRAS*, 505, 4249
 Navarro-Gironés D., et al., 2025, *MNRAS*,

- Newman J. A., et al., 2013, *ApJS*, **208**, 5
1005 Paulin-Henriksson S., Amara A., Voigt L., Refregier A., Bridle S. L., 2008,
A&A, **484**, 67
Planck Collaboration 2020a, *A&A*, **641**, A1
Planck Collaboration 2020b, *A&A*, **641**, A6
Prince H., Dunkley J., 2019, *Phys. Rev. D*, **100**, 083502
1010 Reischke R., et al., 2025, *A&A*, **699**, A124
Rowe B., 2010, *MNRAS*, **404**, 350
Samuroff S., et al., 2023, *MNRAS*, **524**, 2195
Schneider P., van Waerbeke L., Kilbinger M., Mellier Y., 2002, *A&A*, **396**, 1
Schneider P., Eifler T., Krause E., 2010, *A&A*, **520**, A116
1015 Schneider P., et al., 2022, *A&A*, **664**, A77
Schöneberg N., 2024, *JCAP*, **06**, 006
Scodellaggio M., et al., 2018, *A&A*, **609**, A84
Secco L. F., et al., 2022, *Phys. Rev. D*, **105**, 023515
Sheldon E., 2015, Astrophysics Source Code Library, p. ascl:1508.008
1020 Sheldon E. S., Huff E. M., 2017, *ApJ*, **841**, 24
Singh S., Mandelbaum R., 2016, *MNRAS*, **457**, 2301
Singh S., Mandelbaum R., More S., 2015, *MNRAS*, **450**, 2195
Takada M., Hu W., 2013, *Phys. Rev. D*, **87**, 123504
Takada M., Jain B., 2009, *MNRAS*, **395**, 2065
1025 Takahashi R., Sato M., Nishimichi T., Taruya A., Oguri M., 2012, *ApJ*, **761**, 152
Tessore N., Loureiro A., Joachimi B., von Wietersheim-Kramsta M., Jeffrey N., 2023, *Open J. Astrophys.*, **6**, 11
Troxel M. A., et al., 2018, *MNRAS*, **479**, 4998
1030 Van Waerbeke L., et al., 2000, *A&A*, **358**, 30
Wittman D. M., Tyson J. A., Kirkman D., Dell’Antonio I., Bernstein G., 2000, *Nature*, **405**, 143
Wright A. H., Hildebrandt H., van den Busch J. L., Heymans C., 2020, *A&A*, **637**, A100
1035 Wright A. H., et al., 2024, *A&A*, **686**, A170
Wright A. H., et al., 2025a, *arXiv e-prints*, p. arXiv:2503.19441
Wright A. H., et al., 2025b, *A&A*, **703**, A144
Zhang T., et al., 2023, *MNRAS*, **525**, 2441
Zuntz J., et al., 2015, *Astron. Comput.*, **12**, 45
1040 van den Busch J. L., et al., 2020, *A&A*, **642**, A200

APPENDIX A: VALIDATION OF GLASS MOCKS

We present validation tests using the GLASS galaxy mock catalogues. The redshift distribution of the mocks agrees with the data (Fig. A1), as expected. However, since the $n(z)$ distributions of the mocks were not estimated with SOMs, we expect no redshift calibration bias, i.e. $\Delta z = 0$. Nevertheless, we include this as a nuisance parameter that we sample over in the inference step.

We present the recovered Ω_m , σ_8 , and S_8 values from both the configuration-space and Fourier-space pipelines. Fig. A2 shows the distribution of mean posterior values of Ω_m and σ_8 for the configuration-space pipeline; the fiducial values are recovered within 1σ . Fig. A3 shows the distribution of S_8 differences between the Fourier- and configuration-space pipelines across all mocks; the distribution is consistent with a Gaussian centred on zero, validating both pipelines.

APPENDIX B: ADDITIONAL INFERENCE RESULTS

This paper has been typeset from a $\text{\TeX}/\text{\LaTeX}$ file prepared by the author.

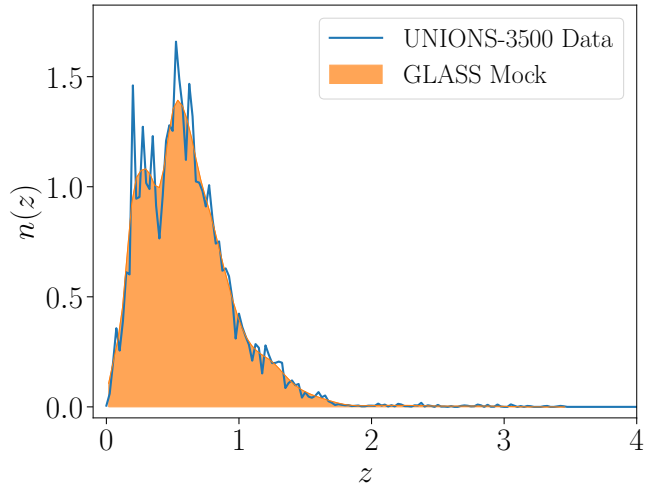


Figure A1. Redshift distribution $n(z)$ of the UNIONS data (blue) and the mock catalogues (orange).

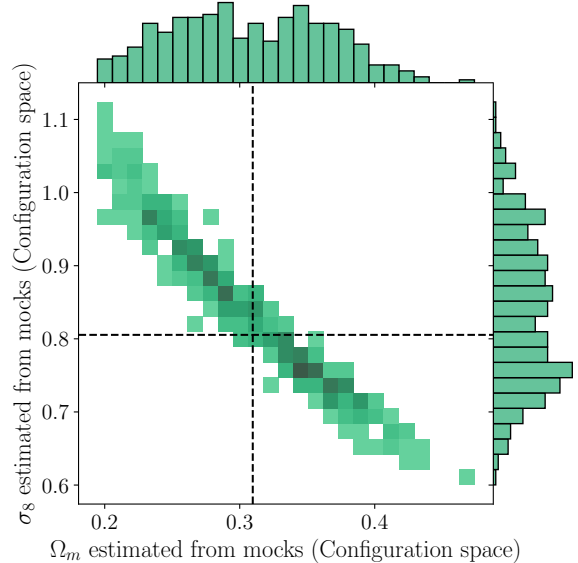


Figure A2. 2D histogram of the recovered mean values in the Ω_m – σ_8 plane, for the configuration space analysis. The fiducial values of the parameters have been marked out in dashed lines. To be updated.

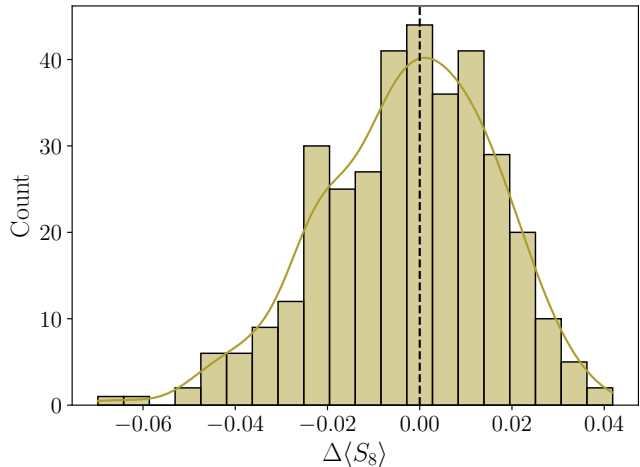


Figure A3. Histogram of the differences in recovered S_8 mean values between the configuration and harmonic space inference pipelines, when run on the 350 mock catalogues. [To be updated](#).